

## Research Paper

# Thermal effects of nonlinear acoustic-gravity waves propagating at thermospheric temperatures matching high and low solar activity

Nikolai M. Gavrilov<sup>a,\*</sup>, Sergey P. Kshevetskii<sup>b</sup>, Andrey V. Koval<sup>a</sup>

<sup>a</sup> Atmospheric Physics Department, Saint-Petersburg State University, Saint Petersburg, Russia

<sup>b</sup> Institute of Physical and Mathematical Sciences and Information Technology, Immanuel Kant Baltic Federal University, Kaliningrad, Russia

## ARTICLE INFO

Presented high-resolution numerical modeling showed that conditions of propagation and characteristics of AGWs excited at the Earth's surface and coming to the thermosphere are depending on modifications in the mean density, temperature, molecular heat conduction, viscosity and composition caused by variations of solar activity. This corresponds to previous research (e.g., Hickey, 1987; Klausner et al., 2009; Vadas and Fritts, 2006; Yiğit and Medvedev, 2010). The present modeling reveals larger amplitudes of AGW temperature perturbations at heights above 150 km at high SA. This might be associated with longer vertical wavelengths and smaller dissipation of temperature perturbations at high SA.

**Keywords:**

Acoustic-gravity waves  
Solar activity  
Thermosphere  
Wave propagation  
Numerical simulation  
Wave heat influx

## ABSTRACT

Numerical high-resolution modeling of nonlinear acoustic-gravity waves (AGWs) generated at the Earth's surface and propagating to the thermosphere shows that wave characteristics are depending on modifications in the mean density, temperature, molecular dissipation and composition due to variations of solar activity (SA). Amplitudes of temperature wave perturbations are generally larger at high SA at altitudes above 150 km, due to larger mean temperature and smaller molecular heat conductivity. Increasing kinematic coefficients of molecular heat conduction and viscosity result in stronger decreasing AGW amplitudes at altitudes larger 150 km at low SA. Dissipating AGWs generally produce heating at altitudes below 120 km. At larger heights, AGWs generally heat the thermosphere at low SA and cool it at high SA. Wave enthalpy fluxes are mainly upwards below 120 km altitude and downwards above 150 km at high SA, where they may have directions opposite to the upward wave energy fluxes. Downward wave enthalpy fluxes correspond to AGW cooling the upper atmosphere at high SA. Nonlinear dissipating AGWs may produce upward and downward transport of atmospheric mass. These mass flows may produce adiabatic heat influxes in the upper atmosphere. Mainly positive residual wave-induced mass flows at altitudes higher 150 km may contribute to the wave cooling of the upper atmosphere. Wave breaking and interactions between waves and the mean flow in the nonlinear model are stronger at higher amplitudes of AGW excitation at the ground, which lead to bigger energy losses for larger-amplitude waves. At high SA, resulting effects in the thermosphere depend on the balance between, on one hand, increases in wave amplitudes, caused by weaker molecular dissipation and smaller transfer of the wave energy to the wave-induced jet flows, and, on the other hand, decreases in the amplitudes due to higher density and larger AGW reflection. The thermal effects of waves in the upper atmosphere may depend on competitions between heating due to dissipation of the upward wave energy flux and cooling due to divergence of the downward wave entropy (or potential enthalpy) flux. At high SA, larger mean temperatures and larger temperature perturbations might increase magnitudes of downward wave entropy fluxes, which may result in more frequent downward wave enthalpy fluxes and wave cooling of the upper atmosphere.

## 1. Introduction

Numerous observations reveal continuous existence of acoustic-gravity waves (AGWs) at altitudes of the middle and upper atmosphere (e.g., Fritts and Alexander, 2003). AGWs are frequently detected in the thermosphere (e.g., Park et al., 2014; Djuth et al., 2004). General circulation models (GCMs) of the atmosphere show that AGWs could propagate to the thermosphere from the lower layers of the Earth's atmosphere (e.g., Yiğit and Medvedev, 2009, 2012; 2015; Yiğit et al., 2014) and at the other planets (e.g., Yiğit and Medvedev, 2016, 2017).

Non-hydrostatic high-resolution models are frequently used for AGW studies. Baker and Schubert (2000) numerically studied nonlinear AGWs in the Venus atmosphere. Studies by Fritts et al. (1996), Andreassen et al. (1998) and Fritts et al. (2009, 2011) utilized two-dimension numerical models for studying Kelvin-Helmholtz instabilities, AGW breaking and generation of atmospheric turbulence. They simulated waves and turbulence in three-dimension regions of the atmosphere with limited horizontal and vertical dimensions. Their numerical algorithms were based on the Galerkin-type expansions for converting partial differential equations into sets of ordinary differential equations

\* Corresponding author.

E-mail address: [n.gavrilov@spbu.ru](mailto:n.gavrilov@spbu.ru) (N.M. Gavrilov).

<https://doi.org/10.1016/j.jastp.2020.105381>

Received 19 December 2019; Received in revised form 30 May 2020; Accepted 6 July 2020

Available online 16 July 2020

1364-6826/© 2020 Elsevier Ltd. All rights reserved.

describing the coefficients of the components of spectral series. Liu et al. (2009) simulated the propagation of AGWs and developing Kelvin-Helmholtz instabilities near the mesopause. AGW propagations in the atmosphere were studied with a two-dimensional numerical model by Liu et al. (2008) and Yu and Hickey (2007).

Several simulations were devoted to AGW effects the middle and upper atmosphere. Hickey et al. (2001) showed that acoustic waves (AWs) might create substantial heating of the upper atmosphere. Lin et al. (2017) made simulations of AGWs generated by random sources near the ground and propagating to the upper atmosphere. They found that AGWs could cause variations of several percent in neutral and electron density. Snively and Pasko (2008) analytically and numerically studied AGWs in the atmosphere. The results showed that short period ducted AGWs might be enforced in the lower thermosphere by wave sources located in the troposphere due to nonlinear processes.

AGWs upcoming from the lower atmosphere to the thermosphere were studied with GCMs (e.g., Yiğit et al., 2012a, 2014, 2017) involving a whole atmosphere parameterization of impacts of saturated and dissipated atmospheric AGWs developed by Yiğit et al. (2008). Applying this parameterization to a numerical model of Martian general circulation revealed that AGWs could propagate from the troposphere to the thermosphere (Medvedev et al., 2013; Yiğit et al., 2015a). This model was successfully applied for interpreting AGWs detected with the MAVEN spaceship in the Martian thermosphere (Yiğit et al., 2015b).

AGWs could propagate from the lower atmosphere, become unstable and produce turbulence at high altitudes. Tropospheric mesoscale turbulent and convective motions might produce AGWs (e.g., Fritts and Alexander, 2003; Fritts et al., 2006). Turbulent wave excitation could be enhanced in jet streams having maxima near the tropopause (e.g., Gavrilov and Fukao, 1999; Medvedev and Gavrilov, 1995; Gavrilov, 2007). Non-hydrostatic modeling of the thermosphere-ionosphere general circulation showed constant AGW presence at thermospheric heights (e.g. Yiğit et al., 2012b).

Gavrilov and Kshevetskii (2013a) developed a two-dimensional high-resolution model utilizing basic conservation laws to simulate nonlinear atmospheric AGWs. This model permitted non-smooth solutions to nonlinear AGW equations and granted the necessary stability of the numerical algorithm (Kshevetskii and Gavrilov, 2005). A three-dimensional kind of this scheme was made by Gavrilov and Kshevetskii (2013b, 2014a) for modeling nonlinear AGWs in the atmosphere. The model was used to simulate waves enforced by monochromatic AGW sources at the Earth's surface. Karpov and Kshevetskii (2014) exploited similar numerical model for studying infrasound excited by localized non-stationary wave sources at the ground and obtained substantial thermal effects of infrasound waves in the thermosphere. Decaying AGWs propagating upwards may also produce wave accelerations of the mean flow at high altitudes (e.g., Fritts and Alexander, 2003). Therefore, peculiarities of thermal and dynamical effects of atmospheric nonlinear non-stationary AGWs require further studies.

Numerous evidences of the solar activity (SA) influence on AGW characteristics in the upper atmosphere exist (e.g., Klausner et al., 2009; Gavrilov, 1995; Yiğit and Medvedev, 2010). SA can vary the solar radiation absorption and change the temperature, density, dissipation and static stability, which can modify conditions of AGW propagation in the thermosphere. Changes in wave characteristics in the hot and cold thermosphere were studied previously (e.g., Hickey, 1987; Yiğit and Medvedev, 2010). Numerical modeling of wave propagations from convective sources in the lower atmosphere to the thermosphere at temperature profiles corresponding to different SA levels (Vadas, 2007; Vadas and Fritts, 2006; Fritts and Vadas, 2008) revealed better conditions for AGW propagation at higher SA because of reduced dissipation. However, larger wave reflections due to increased temperature gradients could compensate easier conditions of AGW propagation. Such conclusions agree with earlier research (Richmond, 1978; Francis, 1973; Gavrilov et al., 1994).

Using a high-resolution model, Gavrilov et al. (2018) simulated the propagation of nonlinear AGWs from the ground wave sources to the upper atmosphere at background vertical profiles of temperature, molecular weight, density, molecular viscosity and heat conduction corresponding to various SA levels. They utilized AGW sources matching with spectral components of the vertical velocity at the surface and compared AGW characteristics and wave dynamical effects at various altitudes in the thermosphere at different SA levels. Gavrilov et al. (2018) showed that AGW velocity amplitudes at altitudes above 150 km are generally larger during high SA because of smaller molecular viscosity and heat conduction. Wave accelerations of the mean velocity by decaying AGWs are generally greater at low SA level. This leads to faster enhancements of wave-induced jet flows at low SA. Net results of SA increases at a given altitude in the thermosphere depend on competitions between the increases in AGW amplitudes caused by decreasing molecular dissipation and decreasing transfer of wave energy to the mean flow and the decreases in the amplitudes due to increased atmospheric density and increased wave reflection.

In the present paper, we continue discussed above study by Gavrilov et al. (2018) and analyze differences in thermal effects of AGWs propagating from the ground wave sources to the thermosphere at the mean temperature profiles corresponding to high and low SA levels using the high-resolution atmospheric wave model by Gavrilov and Kshevetskii (2013b, 2014a). Nonlinear model includes wave-mean flow and wave-wave interactions, which could cause the transfer of energy from the primary wave to the mean flow and to secondary AGWs. Changes in these processes at variable SA could modify wave parameters in the upper atmosphere in addition to differences in AGW dissipation and reflection.

## 2. Numerical model

In this paper, we use the high-resolution model "AtmoSym" for three-dimensional simulation of AGWs in the atmosphere, which was made by Gavrilov and Kshevetskii (2013b, 2014a,b). Recently, the model is available online for all users to make free simulations (AtmoSym, 2016). The AtmoSym model uses the Cartesian geometry for three-dimensional simulations at high horizontal and vertical resolution. Used in the AtmoSym set of primitive three-dimensional equations of motion, continuity and thermal balance is accounting dissipative and nonlinear processes influencing atmospheric AGW propagation (Gavrilov and Kshevetskii, 2013b, 2014a). The model can particularly simulate such complicated phenomena as wave instabilities and generation of turbulence (e.g., Kshevetskii and Gavrilov, 2005).

The AtmoSym model allows a self-consistent depiction of wave processes involving modifications in atmospheric parameters caused by the transfer of energy from decaying AGWs to the atmosphere. Vertical background profiles of the temperature,  $T_0(z)$ , are captured from the atmospheric semi-empirical model NRLMSISE-00 (Picone et al., 2002). The mean molecular heat conductivity,  $\lambda_0$ , and dynamic viscosity,  $\eta_0$ , are estimated using the Sutherlands formula

$$\eta_0 = \frac{1.46 \times 10^{-6} \sqrt{T_0}}{1 + 110/T_0} \left( \frac{kg}{m \cdot s} \right) \quad (1)$$

$$\lambda_0 = \frac{\eta_0}{Pr_m}; Pr_m = \frac{4\gamma}{9\gamma - 5},$$

where  $\gamma = c_p/c_v$  is the ratio of air heat capacities at constant pressure and volume,  $Pr_m$  is the molecular Prandtl number (Kikoin, 1976). In addition, the AtmoSym model involves the mean vertical profiles of turbulent diffusion, which have maxima of  $10 \text{ m}^2\text{s}^{-1}$  near the Earth's surface and at 100 km altitude besides a minimum of  $0.1 \text{ m}^2\text{s}^{-1}$  in the stratosphere (see Gavrilov and Kshevetskii, 2013b, 2014a).

The upper boundary of the model is set at  $z \approx 600$  km, where vertical velocity and vertical gradients of other hydrodynamic parameters are equal to zero (Gavrilov and Kshevetskii, 2014a,b). These conditions

could lead to partial reflections of AGWs propagating from below. Estimations reveal that such reflected AGWs are negligible at altitudes lower than 400–450 km because of small density and high wave dissipation. In this paper, we made computations in a three-dimension atmospheric area and suppose periodicity of wave excitation and solutions at horizontal boundaries of the model (see Gavrilov and Kshevetskii, 2014a). The lower boundary conditions at the ground involve zero vertical gradients of pressure, density and temperature and zero horizontal velocity. AGW modes are excited at the lower boundary with horizontally moving periodical vertical velocity perturbations at the ground having the following form:

$$w_{z=0} = W_0 \cos(\sigma t - \vec{k} \cdot \vec{s}), \quad (2)$$

where  $\vec{k} = (k_x, k_y)$  is the horizontal wave number,  $k_x$  and  $k_y$  are components directed in the horizontal axes  $x$  and  $y$ , respectively,  $\sigma$  is the observable frequency,  $\vec{s} = (x, y)$  is the horizontal radius-vector,  $W_0$  is the amplitude of the analyzed wave mode at the surface. The plane wave sources (2) can correspond to spectral components of convective and turbulent perturbations, which could generate atmospheric AGWs (Townsend, 1965, 1966). Considerations of AGW excitation by atmospheric turbulent and meteorological motions (e.g., Medvedev and Gavrilov, 1995) revealed a wide variety of wavelengths, periods, amplitudes and the other AGW parameters.

Variable SA leads to substantial modifications in the background fields, which could change conditions of AGW propagation, especially in the upper atmosphere. Within the NRLMSISE-00 model, SA variations are specified by values of the solar  $F_{10.7}$  flux of radio waves having length of 10.7 cm (Picone et al., 2002). In this study, we use vertical profiles of the mean density,  $\rho_0$ , temperature,  $T_0$ , atmospheric molecular weight,  $\mu$ , and kinematic viscosity,  $\nu = \eta_0/\rho_0$ , which are the same as ones used by Gavrilov et al. (2018). They are presented in Fig. 1 of the paper by Gavrilov et al. (2018) and are generated by the NRLMSISE-00 for noon January 15 at latitude of 50°N for values of  $F_{10.7} = 70, 120, 250$  sfu matching, respectively, to the low, medium and high SA. These profiles represent typical differences of the background fields between different SA levels at middle latitudes. They show that at low SA  $T_0, \rho_0, \mu$  are much

smaller and  $\nu$  is larger than the respective values at high SA in the upper atmosphere. Impacts of these differences on AGW thermal effects are studied below.

The numerical simulations are performed for the background profiles of  $T_0, \rho_0, \mu$  and  $\nu$  taken from the NRLMSISE-00 model (see above), which do not change during the AtmoSym runs for each SA level. Modeling starts from unperturbed atmosphere with zero wind and zero disturbances of other hydrodynamic fields. Simulations were made for the surface wave forcing (2) with various horizontal phase speeds  $c_x \sim 30$ –100 m/s, amplitudes  $W_0 \sim 0.1$ –1 mm/s and the wave period  $\tau = 0.56$  h. Horizontal wavelengths  $\lambda_x = c_x \tau \sim 60$ –200 km and horizontal dimensions of simulated domain are  $L_x = 4\lambda_x$ . The model grid contains 64 nodes per horizontal wavelength and 1024 nodes vertically in the altitude range of 0–600 km. Time step (less than a few seconds) and vertical grid spacing are determined automatically depending on the horizontal wavelength and vertical inhomogeneity of the background profiles.

The model computes deviations of atmospheric pressure, temperature and density from their background values, and velocity components. In linear models, these deviations represent wave variations of atmospheric parameters. In nonlinear models, deviations from background profiles may contain wave-induced changes in the mean fields. In the present simulations, background fields and parameters of wave sources (2) are stationary and horizontally homogeneous. Therefore, wave-induced changes in the mean fields may be obtained by averaging simulated deviations over one wavelength in horizontal plane at every altitude and time step. In the AtmoSym model, such wave-induced mean values participate in further simulations and can be considered as additions to the background fields. Wave components may be obtained as differences between simulated deviations and the wave-induced changes in the mean values for each hydrodynamic quantity.

Previous studies with the AtmoSym model (e.g., Gavrilov and Kshevetskii, 2014a; b, 2015) revealed that abrupt triggering the ground plane wave forcing (2) may excite an initial wave pulse, which during 5–10 min can reach altitudes of 100–200 km. To smooth the wave source activation, the forcing (2) at times  $t < t_0$  was multiplied by factor

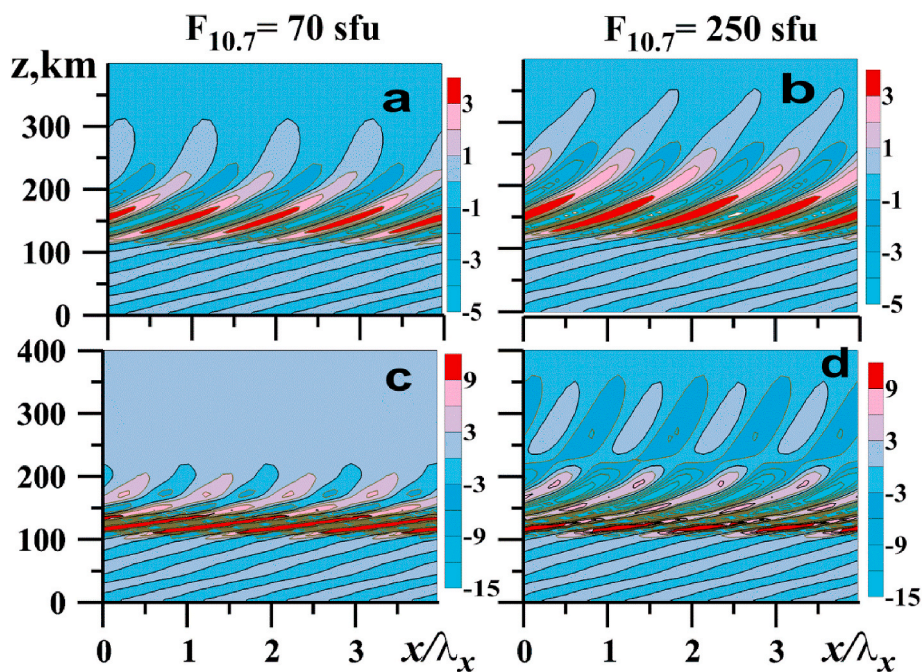


Fig. 1. Distributions of simulated temperature deviations (in K) in the plane XOZ with the axis  $x$  directed along the horizontal wave vector  $\vec{k}$  at time  $t = 9\tau$  for values of solar radiowave flux  $F_{10.7} = 70$  sfu (left) and  $F_{10.7} = 250$  sfu (right) at the amplitudes  $W_0 = 0.1$  mm/s (a,b) and  $W_0 = 1$  mm/s (c,d), period  $\tau = 0.56$  h,  $c_x = 100$  m/s and  $\lambda_x = 200$  km of the surface wave source (2) and interval of wave activation  $t_0 = 1$  s in (3).

$$r(t) = \begin{cases} \exp[-(t-t_0)^2/d^2] & \text{at } t \leq t_0 \\ 1 & \text{at } t > t_0 \end{cases}, \quad (3)$$

where parameters  $d$  and  $t_0$  define the rate and duration of the source activation interval. In this study, the parameters of (3) were changed inside the range of  $t_0 \sim 1-10^3$  s with  $d = t_0/3$ . The smoothing (3) allows diminishing initial AGW pulses appearing during the wave source activating.

### 3. Simulation results

We executed modeling of nonlinear waves propagating to the middle and upper atmosphere from a plane AGW source at the ground (2) at the wave period  $\tau = 0.56$  h.

#### 3.1. AGW amplitudes and energy flux

After triggering the ground AGW source at  $t = 0$ , an initial package of acoustic and extremely long gravity wave components needs a few minutes to arrive at altitudes above 100 km (e.g., Gavrilov and Kshevetskii, 2014b). After dissipating and spreading this initial wave package, slower internal gravity waves (IGWs) matching to the period of the ground wave excitation (2) reach the upper atmosphere heights (Gavrilov and Kshevetskii, 2015). Fig. 1 depicts distributions of simulated deviations of temperature from the background profiles in the vertical plane, having horizontal  $x$ -axis directed parallel to the horizontal wave vector  $\vec{k}$ , at the moment  $t = 9\tau$  for various values of  $F_{10.7}$  solar flux and various amplitudes  $W_0$  of the ground wave excitation (2) for the sharp AGW source activating at  $t_0 = 1$  s in (3). At heights below 100 km in Fig. 1, wave fronts are tilted to the horizon, which should match with atmospheric IGWs (Gossard and Hooke, 1975). Tilts of the wave fronts to the horizon become larger in the thermosphere in Fig. 1, because of reducing vertical wave numbers due to large molecular heat conductivity and viscosity (e.g., Gavrilov and Shved, 1975).

Comparing Fig. 1a and c for the AGW source amplitudes  $W_0 = 0.1$  mm/s and  $W_0 = 1$  mm/s in (2) reveals layers of small-scale temperature perturbations at heights of 100–150 km, which are stronger in Fig. 1c. This can be connected with stronger convective and dynamical instabilities of large-amplitudes IGWs in this altitude region (e.g., Gavrilov and Kshevetskii, 2015). Fig. 1 shows that this instability and small-scale temperature perturbations at altitudes 100–150 km are stronger at high SA. Previous modeling by Gavrilov et al. (2018) revealed that wave breaking could result in wave-induced jet flows having the mean wind velocity reaching the horizontal wave phase speed,  $c_x$ . Enhanced transition of energy from the wave to the mean flow and wave dissipation may produce a decrease in IGW amplitudes at higher altitudes, which should be larger for higher-amplitude IGWs. Ratios of IGW amplitudes presented in Fig. 1c and d to the respective quantities shown in Fig. 1a and b at altitudes near 150 km are about 3, which is significantly smaller than the ratio 10 of the respective amplitudes of the ground wave excitation (2). This corresponds to similar results obtained for the amplitudes ratio of the vertical velocity wave variations in Table 1 of the paper by Gavrilov et al. (2018).

Fig. 2 shows vertical profiles of temperature deviations at the moment  $t = 55\tau$  after the wave source triggering for various phases at different locations along the horizontal axis  $x$  within one IGW period. Sixty-four shifted individual profiles are overlapping and look like shaded regions in Fig. 2, which give information on ranges of temperature deviations at different altitudes. Thick lines in Fig. 2 represent wave-induced changes in the mean temperature obtained by averaging over one wavelength in the horizontal planes at each altitude. Wave amplitudes are equal to the distances from these mean lines to the edges of dark shaded areas at every altitude in Fig. 2.

At weak wave excitation in the top panels of Fig. 2, the widths of shaded areas (corresponding to doubled temperature amplitudes) at

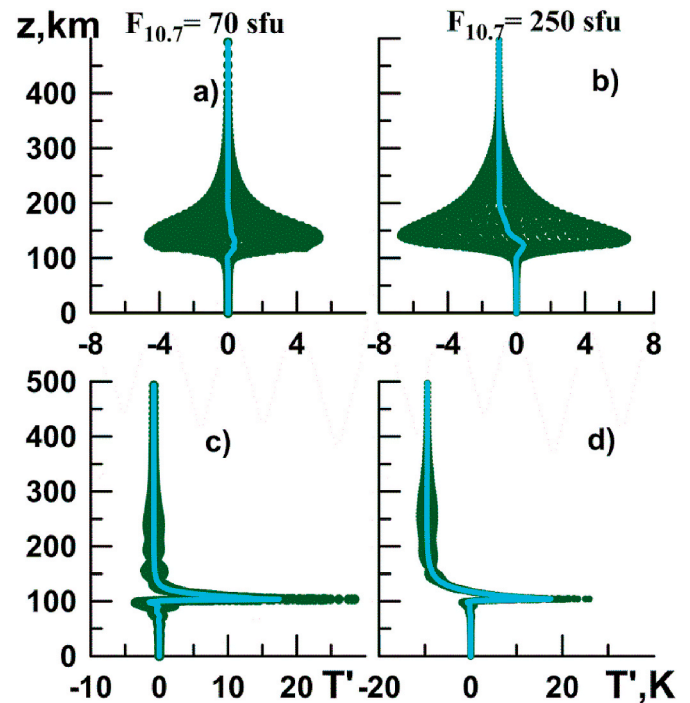


Fig. 2. Vertical profiles of temperature deviations produced by AGW source (2) with period  $\tau = 0.56$  h,  $c_x = 100$  m/s,  $\lambda_x = 200$  km and amplitudes  $W_0 = 0.1$  mm/s (a,b) and  $W_0 = 1$  mm/s (c,d) at time  $t = 55\tau$  for values of solar radiowave flux  $F_{10.7} = 70$  sfu (left) and  $F_{10.7} = 250$  sfu (right). Thick lines show average over horizontal wavelength values for each altitude.

heights 110–200 km are larger at high SA in Fig. 2b, than the respective amplitudes in Fig. 2a for the low SA level. It is opposite to the case of wave amplitudes of vertical velocity perturbations, analyzed by Gavrilov et al. (2018). In the presence of molecular heat conduction, for low frequency short waves with  $\omega^2 \ll N^2$  and  $m^2 \gg 1/(4H^2)$ , the rate of temperature perturbation damping,  $\alpha$ , may be approximated with the following expressions:

$$\alpha = \chi m^2; \chi = \lambda_0/\rho_0; m^2 \approx k^2 N^2/\omega^2; N^2 = g(\partial T_0/\partial z + \gamma_a)/T_0; \gamma_a = g/c_p, \quad (4)$$

where  $m$  and  $k$  are vertical and horizontal wave numbers;  $\omega$  is AGW intrinsic frequency;  $\chi$  is kinematic molecular temperature conductivity;  $N$  is Brunt-Vaisala frequency;  $H$  is atmospheric scale height;  $\gamma_a$  is temperature adiabatic lapse rate;  $g$  is gravity acceleration;  $c_p$  is specific heat capacity at constant pressure (e.g., Gavrilov and Shved, 1975). At altitudes above 150 km,  $\partial T_0/\partial z \ll \gamma_a$ , hence  $N^2 \approx g\gamma_a/T_0$  and  $N^2$  is about 2 times smaller at high SA compared to that at low SA, as far as  $T_0$  at high SA is about 2 times larger than  $T_0$  at low SA in our model (see Fig. 1 in the paper by Gavrilov et al., 2018). Therefore, at the same  $k$ , magnitudes of  $m$  in (4) are smaller at high SA compared to those at low SA. This is noticeable in Fig. 1, where regions of positive and negative temperature perturbations are wider at altitudes above 150 km in Fig. 1b, which corresponds to larger vertical wavelengths at high SA.

Traditional polarization relations for low frequency short IGWs in the non-dissipative atmosphere (e.g., Gossard and Hooke, 1975) give the ratio of wave amplitudes of temperature,  $|T'|$ , and vertical velocity,  $|w'|$ , in the form of  $|T'|/|w'| \sim N^2 T_0/(g\omega)$ . In the dissipative atmosphere,  $|T'|_d/|w'|_d \sim [|T'|/|w'|]\omega/(\omega^2 + \alpha^2)^{1/2}$  (Gavrilov and Shved, 1975). Taking  $N^2 \approx g\gamma_a/T_0$  for altitudes above 150 km (see above), one can get  $|T'|_d/|w'|_d \sim \gamma_a/(\omega^2 + \alpha^2)^{1/2}$ . Values of  $\chi$ ,  $m$  and  $\alpha$  in (4), are smaller at high SA. Therefore, at given altitude and  $|w'|$ , amplitudes of temperature perturbations should be larger at high SA, as it is seen in Fig. 2 at heights larger 150 km. Rising molecular heat conduction and viscosity

result in decreasing temperature amplitudes versus altitude in the top panels of Fig. 2a and b at heights above 150 km.

The bottom panels of Fig. 2c and d for the larger amplitude of the surface AGW excitation  $W_0 = 1$  mm/s depict high amplitudes of temperature perturbations at heights near 100 km. So strong waves become unstable and breaking, which may result in generation of wave-induced jet flows studied by Gavrilov et al. (2018) and displayed in Fig. 3. Velocities of these flows may approach the horizontal phase speed of AGW excitation (2). Hence, wave-induced jet streams may create near-critical layers, where vertical wavelengths of the primary AGW modes propagating from the surface could be substantially decreased leading to the strong dissipation of wave energy (e.g., Gossard and Hooke, 1975). This enhanced dissipation may result in strong decreases of AGW amplitudes at heights 110–150 km in Fig. 2c and d. Above height of 150 km, the wave-induced horizontal flows in Fig. 3 are smaller and allow grows of the amplitude of primary AGW mode tunneling through the near-critical layers.

Time variations of temperature standard deviations  $\delta T$  (proportional to AGW amplitudes) calculated at horizontal planes located at different altitudes are depicted in Fig. 4 for different altitudes. The left panels of Fig. 4 for small amplitude of the surface wave excitation reveal quasi-stationary AGW amplitudes at altitudes below 150 km after the primary wave mode from the surface excitation (2) arrives at the respective height. The arrival time increases at larger heights (Gavrilov and Kshevetskii, 2014b). At altitudes above 150 km, the left panels of Fig. 4 demonstrate gradual  $\delta T$  decreases in time. This might be caused by the wave energy transfer to the wave-induced mean flows (see respective panels of Fig. 3), which are produced at altitudes above 110–120 km and are strengthening in time (Gavrilov et al., 2018).

At heights above 150 km,  $\delta T$  values are greater at high SA in the left panels of Fig. 4, which is opposite to lower standard deviations of vertical velocity at the respective panels of Fig. 5 of the paper by Gavrilov et al. (2018). The reason for larger  $\delta T$  values could be higher mean

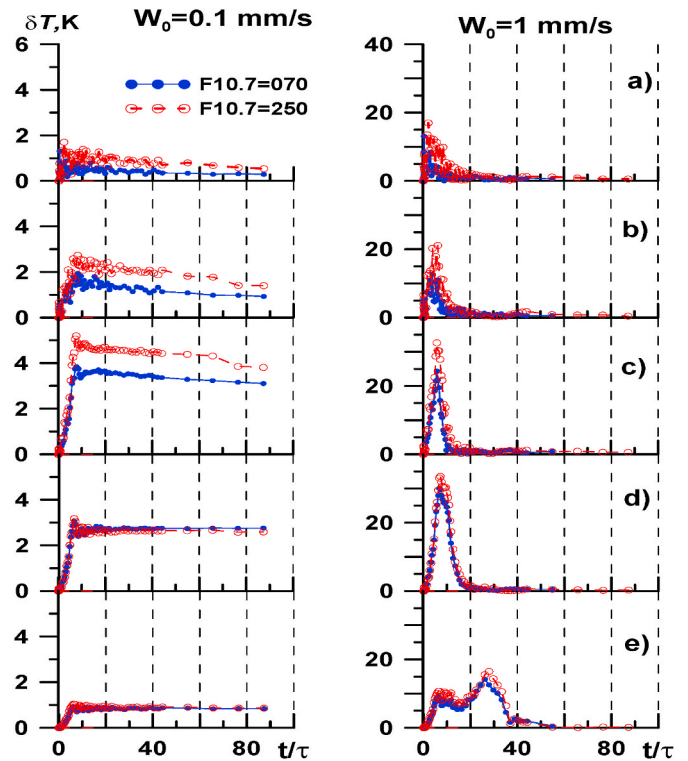


Fig. 4. Similar to Fig. 3, but for simulated standard deviation of temperature.

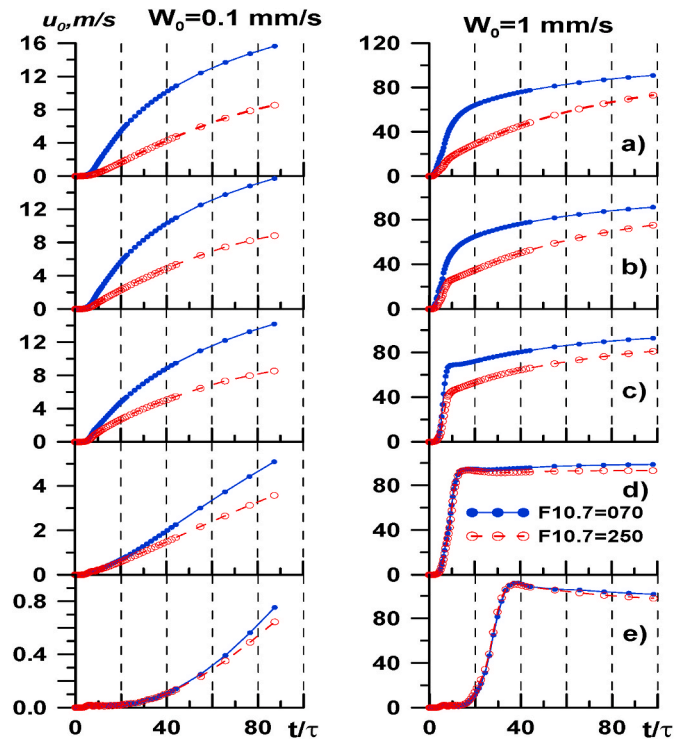


Fig. 3. Temporal variations of simulated wave-induced mean horizontal velocity at altitudes 250 km (a), 200 km (b), 150 km (c), 120 km (d), 110 km (e) for amplitudes  $W_0 = 0.1$  mm/s (left) and  $W_0 = 1$  mm/s (right) of the surface wave forcing (2) with period  $\tau = 0.56$  h,  $c_x = 100$  m/s and  $\lambda_x = 200$  km at low ( $F_{10.7} = 70$  sfu) and high ( $F_{10.7} = 250$  sru) levels of solar activity.

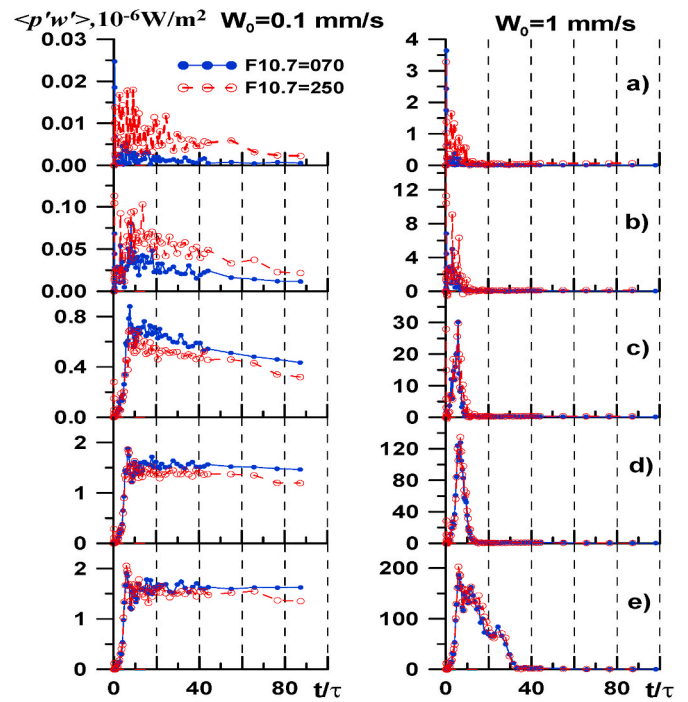


Fig. 5. Similar to Fig. 3, but for the vertical wave energy flux.

temperatures in the thermosphere at high SA, which increases amplitudes of absolute temperature perturbations (see above). In addition, larger molecular heat conduction and viscosity at large heights may lead to larger wave dissipation at low SA. Therefore, differences in  $\delta T$  values at heights 200–250 km for high and low SA become larger in the left panels of Fig. 4.

At larger amplitudes of the wave excitation (2), jet flows induced by

waves in the right panels of Fig. 3 may have speeds approaching the horizontal phase speed of primary wave and may create near-critical layers of strong AGW dissipation (see Gavrilov et al., 2018). This may almost stop upward wave propagation, leading to considerable  $\delta T$  decreases at heights above 100 km in the right panels of Fig. 4 after formation of strong wave-induced flows. Fig. 4e reveals longer interval of substantial values of  $\delta T$  at altitude of 110 km compared to the above heights. Considerations of Fig. 3e show that the wave-induced mean horizontal velocity reaches high values later at altitude of 110 km than that at higher panels of Fig. 3. Therefore, decreasing amplitudes of AGWs propagating from below due to the near-critical levels occur later at 110 km. Fig. 5 shows temporal changes at various heights of the vertical flux of wave energy

$$F_e = \langle p' w' \rangle, \quad (5)$$

where  $p$  and  $w$  are pressure and vertical velocity, sign  $\langle \rangle$  refers to the averaging for AGW period along the horizontal  $x$  axis, primes denote wave perturbations. Changes in  $F_e$  values in Fig. 5 are very similar to respective changes in the wave momentum flux presented by Gavrilov et al. (2018). All  $F_e$  values are positive, which correspond to the upward propagation of wave energy. At small wave source amplitude (the left panels of Fig. 5) at heights lower than 150 km, magnitudes of  $F_e$  are smaller at high SA. This might be connected with stronger reflection of AGW energy at high SA in the region of maximum  $\partial T_0 / \partial z$  and  $N^2$  at altitudes 110–150 km (Walterscheid and Hickey, 2011). Reflected waves have downward energy fluxes, which may decrease upward  $F_e$  fluxes produced by the primary AGW mode below the reflection layers. AGW energy fluxes at altitudes 200–250 km in the left panels of Fig. 5 are larger at high SA, due to larger  $\nu$  and  $\chi$  caused by the lower  $\rho_0$  at low SA. In the right panels of Fig. 5, at higher AGW excitation amplitude,  $F_e$  at heights above 100 km has maximums at  $t \sim (5-10)\tau$ , when jet flows induced by waves in the respective panels of Fig. 3 are weak. Later,  $F_e$  values decrease because of robust dissipation of primary AGWs within the near-critical layers produced by jet flows induced by waves (see above).

### 3.2. AGW thermal effects

Thick lines in Fig. 2 show the wave-induced mean temperature changes  $\Delta T_0$ . They are obtained by averaging simulated temperature deviations over one wavelength in the horizontal plane at each time step. In the AtmoSym model, values of  $\Delta T_0$  may be considered as modifications of the stationary background profiles at any time step, which are participating in the further simulations. One can see maximum increases in the mean temperature at altitudes 100–120 km, where substantial wave instabilities and dissipation take place (see above). The wave heating in this region is larger for high-amplitude IGWs in Fig. 2c and d compared to Fig. 2a and b, respectively. Above the altitude of 150 km, the wave-induced mean temperature changes are positive at low SA at the left panels of Fig. 2 and are negative at high SA at the right panels of Fig. 2. These changes are larger at stronger ground wave excitation (2) in the bottom panels of Fig. 2.

Time variations of the wave-induced mean temperature add-ons,  $\Delta T_0$ , at different altitudes are given in Fig. 6. At altitudes below 150 km,  $\Delta T_0$  values are generally positive in Fig. 6, which corresponds to the atmosphere heating by dissipating AGWs. Above 150 km altitude,  $\Delta T_0$  values are generally positive at low SA and negative at high SA, when AGWs generally cool the upper atmosphere. Magnitudes of the wave heating/cooling are larger at higher amplitude of the surface wave source (2) in the right panels of Fig. 6.

The main contribution to the wave heating rate comes from the divergence of the wave enthalpy flux (e.g., Akmaev, 2007), which is sometimes called as “sensible wave heat flux” (e.g., Hickey et al., 2011),

$$F_t = \rho_0 c_p \langle T' w' \rangle. \quad (6)$$

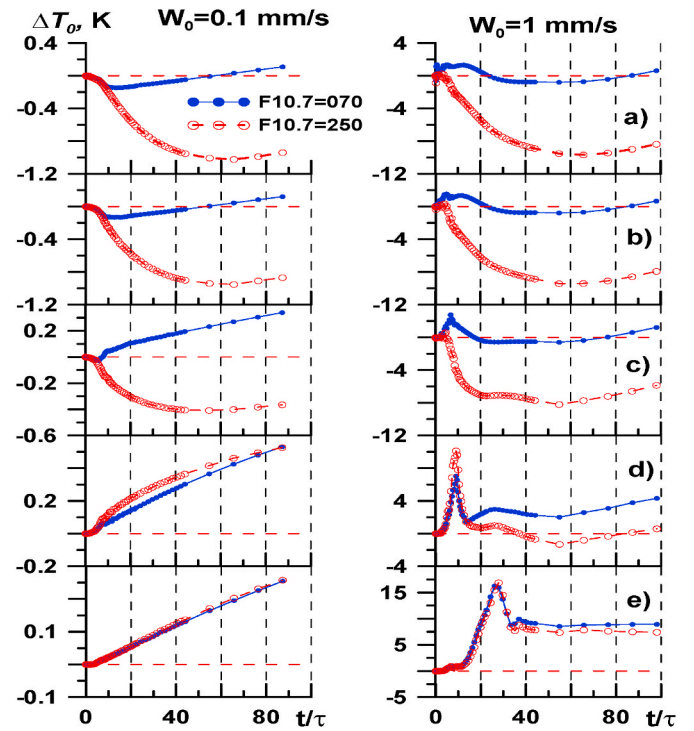


Fig. 6. Temporal variations of simulated wave-induced mean temperature changes at altitudes 250 km (a), 200 km (b), 150 km (c), 120 km (d), 110 km (e) for amplitudes  $W_0 = 0.1$  mm/s (left) and  $W_0 = 1$  mm/s (right) of the surface wave forcing (2) with period  $\tau = 0.56$  h,  $c_x = 100$  m/s and  $\lambda_x = 200$  km at low ( $F_{10.7} = 70$  sfu) and high ( $F_{10.7} = 250$  sru) levels of solar activity. Horizontal dashed lines show zero levels.

Time changes of  $F_t$  values are presented in Fig. 7. IGW theory for hydrostatic hydrodynamic models shows that wave perturbations  $w'$  and  $T'$  have phase shift of  $\pi/2$ , which gives  $F_t = 0$  in the absence of wave dissipation and  $F_t < 0$  in the dissipative atmosphere (e.g., Medvedev and Klaassen, 2003). For non-hydrostatic equations, in classical model of

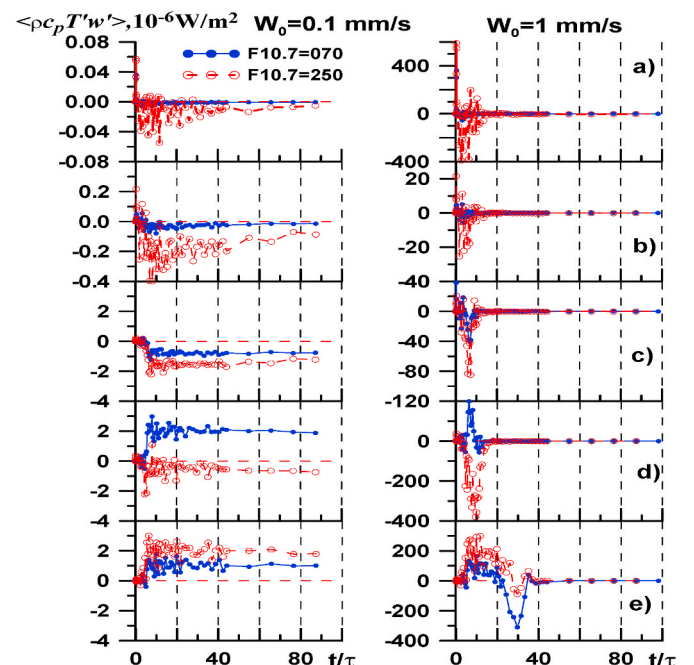


Fig. 7. Similar to Fig. 6, but for the vertical wave enthalpy flux.

isothermal atmosphere and stationary horizontal homogeneous regime of non-dissipating waves, the phase shift between  $w'$  and  $T'$  variations is different from  $\pi/2$  and AGW polarization relations (e.g., Gossard and Hooke, 1975) lead to the relation

$$F_t = F_e \quad (7)$$

Therefore, one may expect positive values of the wave enthalpy flux in Fig. 7 corresponding to the upward  $F_e$  in Fig. 5. However, Fig. 7 demonstrates many negative  $F_t$  values, especially, at high SA. Below 120 km altitude,  $F_t$  values are mainly positive in Fig. 7e, which draws a parallel with positive  $\Delta T_0$  in Fig. 6e. At altitudes above 150 km in Fig. 7a–c, the  $F_t$  values are mostly negative at high SA, showing downward directions of the wave enthalpy flux opposite to the upward directions of the wave energy flux in Fig. 5a–c. Negative  $F_t$  in Fig. 7a–e corresponds to stronger AGW cooling of the upper atmosphere at high SA shown in Fig. 6a–c. Possible reasons for the discrepancies between  $F_t$  and  $F_e$  values are discussed in section 4.

### 3.3. Vertical mass flows

Substantial differences between magnitudes of the wave fluxes of enthalpy (6) and energy (5), discussed above, may reflect substantial changes in the transport of atmospheric mass by AGWs, which is described by the wave mass flux

$$F_\rho = \langle \rho' w' \rangle. \quad (8)$$

Fig. 8 represents time variations of the wave mass flux at different altitudes. Most  $F_\rho$  values are positive in Fig. 8 showing upward mass transport by AGWs. At altitudes higher than 200 km,  $F_\rho$  values are larger at high SA in Fig. 8a and b. Below 200 km, ratios of  $F_\rho$  magnitudes at high and low SA could be different at different altitudes in Fig. 8c–e.

Wave mass fluxes (8) in the atmosphere could be compensated by the mass transport with the mean vertical velocity  $w_0$ . In the nonlinear model, dissipating AGWs can modify  $w_0$  values making changes in the mean mass fluxes. In the AtmoSym model, the background vertical velocity is zero, and model  $w_0$  values represent the wave-induced vertical velocities, which are depicted in Fig. 9. Most  $w_0$  values are negative in Fig. 9. In most cases, downward mean vertical velocities are stronger at

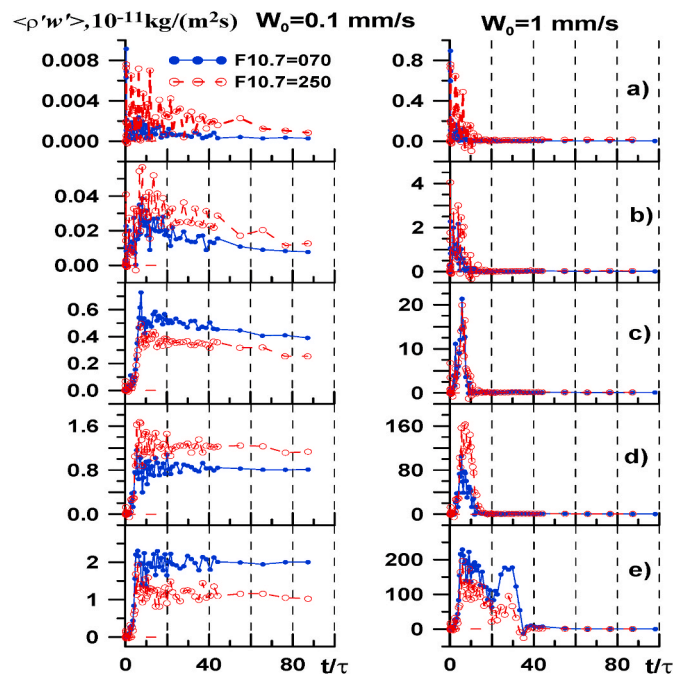


Fig. 8. Similar to Fig. 6, but for the vertical wave mass flux.

low SA. Generally opposite signs of  $F_\rho$  in Fig. 8 and  $w_0$  in the respective panels of Fig. 9 show a partial compensation of vertical wave mass fluxes by wave-induced mean vertical flows. Therefore, the effective speed,  $w_m$ , of the residual vertical mass transport produced by AGWs could be estimated as

$$w_m = w_0 + F_\rho / \rho_0. \quad (9)$$

Time variations of simulated  $w_m$  are presented in Fig. 10. One can see that nonlinear dissipating IGWs may produce upward and downward residual transport of atmospheric mass. The heat balance equation for the mean atmospheric state (e.g., Akmaev, 2007) contains the adiabatic heating rate

$$\varepsilon_a = -w_m (\partial T_0 / \partial z + \gamma_a). \quad (10)$$

Therefore, negative  $w_m$  values in Fig. 10 correspond to heating and positive  $w_m$  correspond to cooling of the atmosphere. Shown in Fig. 10 values of  $|w_m| \sim 0.01\text{--}10 \text{ cm/s}$  correspond to the adiabatic heating rates  $|\varepsilon_a| \sim 0.1\text{--}100 \text{ K/day}$ . In the right panels of Fig. 10 for the surface wave excitation amplitude  $W_0 = 1 \text{ mm/s}$ , the  $w_m$  values are mainly positive at altitudes higher 150 km. Therefore, the wave-induced vertical transport of atmospheric mass may contribute to the cooling the upper atmosphere by AGWs.

### 4. Discussion

Considered above modeling was performed for the surface wave excitation (2) with amplitudes  $W_{01} = 0.1 \text{ mm/s}$  and  $W_{02} = 1 \text{ mm/s}$ . Within the linearized AGW model, proportionality between the amplitude of the wave excitation and wave amplitudes at all heights should be expected. Wave breaking and interactions between waves and the mean flow in the nonlinear model are stronger at higher surface AGW excitation amplitudes, leading to relatively bigger energy losses for larger-amplitude waves. Our analysis (see description of Fig. 1) shows that at high altitudes the ratios of wave temperature amplitudes, energy and enthalpy fluxes produced by waves with the excitation amplitudes  $W_{01}$  and  $W_{02}$  are much smaller compared to  $W_{02}/W_{01} = 10$  for the wave amplitudes and smaller than  $(W_{02}/W_{01})^2 = 100$  for the wave fluxes. This

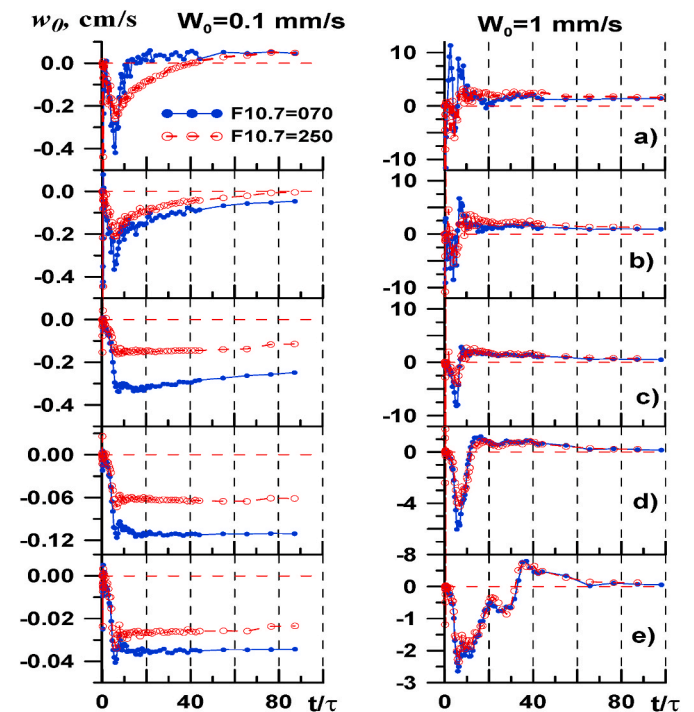


Fig. 9. Similar to Fig. 6, but for the wave-induced vertical mean velocity.

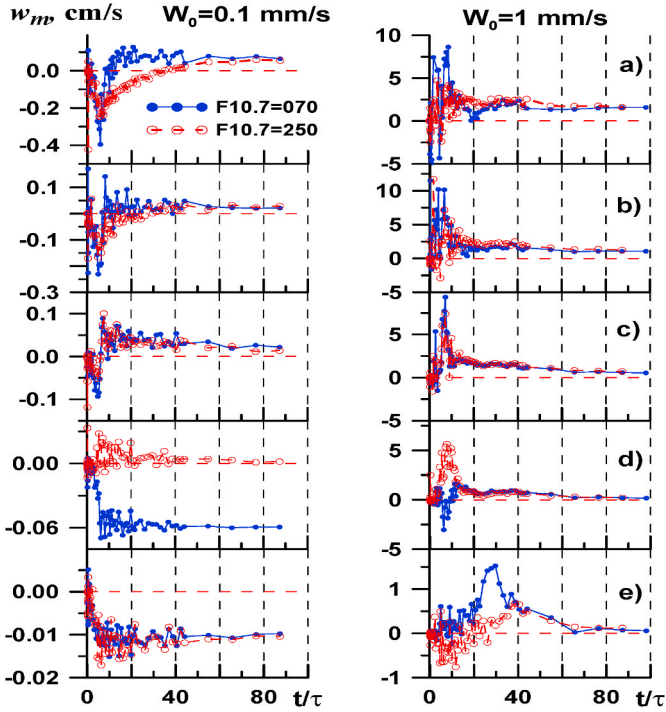


Fig. 10. Similar to Fig. 6, but for the effective vertical velocity of residual mass transport.

result is similar to that shown in Table 1 of the paper by Gavrilov et al. (2018).

Mentioned above smaller ratios of amplitudes may be connected with larger dissipation and energy losses for larger-amplitude AGWs. Additional decreases of AGW amplitude may come from strong reflections of waves propagating from below in the layers of big vertical shears of the mean temperature at heights 110–150 km (Walterscheid and Hickey, 2011; Yiğit and Medvedev, 2010). Gradients of temperature and the wave reflection are stronger at high SA (Hickey, 1987; Vadas and Fritts, 2006; Vadas, 2007; Fritts and Vadas, 2008). Hence, final SA effects may depend on balances between, on one hand, increases in AGW amplitudes caused by smaller molecular heat conduction and smaller transfer of wave energy to the wind-induced jet streams and, on the other hand, decreases in the amplitudes due to larger density and wave reflections at higher SA.

Considering AGW thermal effects in a non-hydrostatic model, Akmaev (2007) obtained the following relation between the wave enthalpy (6) and energy (5) fluxes:

$$F_t = F_e + F_\theta; F_\theta = \rho_0 c_p \Pi_0 < \theta' w' >; \Pi = (p/p_s)^k; \theta = T/\Pi, \quad (11)$$

where  $F_\theta$  can be called as the wave flux of potential enthalpy,  $\theta$  is potential temperature,  $p_s$  is the surface pressure,  $\kappa = (c_p - c_v)/c_p$ . According to Eq. (9) of the paper by Gavrilov (1990),  $F_\theta$  is proportional to the wave flux of entropy,  $s$ :

$$F_\theta = \rho_0 T_0 < s' w' >; s' = (c_p T - p')/\rho_0 / T_0. \quad (12)$$

Gavrilov (1990) obtained a relation between  $F_\theta$  and the wave component of the specific heat influx due to dissipative processes,  $\varepsilon'$ ,

$$F_\theta = \rho_0 \gamma_a < \varepsilon s' > / N^2. \quad (13)$$

For non-dissipative AGWs,  $\varepsilon' = 0$  and  $F_\theta = 0$ , therefore, (11) turns into Eq. (7). For AGW dissipation due to molecular heat conduction, Akmaev (2007) derived an expression for  $F_\theta$ , which in the present notations has the following form:

$$F_\theta = -\rho_0 \varepsilon_T H / \kappa; \varepsilon_T = \alpha g^2 < T^2 / T_0^2 > / N^2. \quad (14)$$

As far as  $\varepsilon_T > 0$  at stable stratification, Eq. (14) shows that  $F_\theta < 0$  in dissipative atmosphere. Values of  $F_e$  in (11) are generally positive for AGWs propagating upwards (see Fig. 5). Therefore, the sign of the wave enthalpy flux,  $F_\theta$ , depends on relative values of  $F_e$  and  $F_\theta$ . When  $F_\theta < -F_e$ , the wave enthalpy flux is downwards. Using relations (4), one can change the expression for  $\varepsilon_T$  in (14) to the form of  $\varepsilon_T \approx \chi g^2 k^2 < T^2 / T_0^2 > / \omega^2$ . Wave temperature perturbations are generally larger at high SA in Fig. 4 at altitudes above 150 km. In addition,  $H$  in (14) is also larger at high SA. This might increase magnitudes of negative  $F_\theta$  and may explain the dominance of negative  $F_t$  values in Fig. 7 at altitudes above 150 km at high SA.

Hickey et al. (2011) analyzed AGW heating/cooling rates in the thermosphere. They obtained formulae similar to (14) for the wave enthalpy flux. They showed that for quasi-saturated AGWs the heating rate due to vertical divergence of  $F_t$  is

$$\varepsilon_w = -\rho_0^{-1} \partial F_t / \partial z \approx F_t / (\rho_0 H), \quad (15)$$

because of exponential decreases of atmospheric density in altitude. Therefore, signs of AGW thermal effects depend on vertical directions of the wave enthalpy flux. Equation (15) shows that positive  $F_t$  corresponds to wave heating and negative  $F_t$  matches with cooling the atmosphere by dissipating AGWs. This may explain correlations between  $F_t$  signs in Fig. 7 and the mean temperature changes in Fig. 6. Hickey et al. (2011) also showed that, in addition to the convergence of the wave enthalpy flux, a contribution to the heating/cooling of the atmosphere above 150 km altitude might give the divergence of the viscous flux of wave kinetic energy.

The above discussion shows that AGW thermal effects in the upper atmosphere may depend on competitions between heating due to dissipation of the upward wave energy flux and cooling due to divergence of downward wave entropy (or potential enthalpy) flux. Modifications in the mean temperature, molecular heat conduction and viscosity due to changes in solar activity may change proportions of wave energy and entropy fluxes in (11) and may lead to upward or downward wave enthalpy fluxes, which correspond to heating or cooling the upper atmosphere by AGWs, respectively. Negative  $F_t$  and wave cooling of the upper atmosphere could be more frequent at high SA.

## 5. Conclusion

Higher amplitudes of wave sources on the ground leads to AGW breaking and productions of mesoscale temperature perturbations at heights 100–150 km. Increased decay of breaking waves can generate wave-induced mean flows with velocities up to AGW horizontal phase speeds. High wave decay in near-critical regions made by the wave-induced mean flows at heights 110–150 km substantially diminishes AGW amplitudes, energy and enthalpy fluxes produced by primary waves generated by the wave excitation at the ground. The wave-induced mean horizontal flows become weaker at heights above 150 km, making grows of amplitudes of the partially penetrating primary wave and of AGW secondary modes, which might be generated within the wave-induced mean flows. Such grows of wave amplitudes is smaller at low SA because of larger speeds of wave-induced jet streams and higher molecular heat conduction and viscosity.

The wave-induced mean temperature add-ons,  $\Delta T_0$ , are generally positive below 120 km altitude. At larger heights,  $\Delta T_0$  values are generally positive at low SA and negative at high SA, when AGWs cool the upper atmosphere. Below 120 km altitude, values of the wave enthalpy flux,  $F_t$ , are mainly positive and are mostly negative at high SA at altitudes above 150 km, showing downward directions of the wave enthalpy flux opposite to the upward directions of the wave energy flux in Fig. 5a–c. Negative  $F_t$  values correspond to stronger AGW cooling of the upper atmosphere at high SA. Nonlinear dissipating AGWs may

produce vertical transport of atmospheric mass. These mass flows may produce adiabatic heating rates in the upper atmosphere. Mainly positive wave-induced residual mass flows at altitudes higher 150 km may contribute to the cooling of the upper atmosphere by AGWs. Wave breaking and interactions between waves and the mean flow in the nonlinear model are stronger at higher surface AGW excitation amplitudes, leading to bigger energy losses for larger-amplitude waves.

Wave thermal effects in the upper atmosphere may depend on competitions between heating due to dissipation of the upward wave energy flux and cooling due to divergence of downward wave entropy (or potential enthalpy) flux. At high SA, larger mean values and wave perturbations of temperature may increase magnitudes of downward wave entropy fluxes, and may result in more frequent downward wave enthalpy fluxes corresponding to wave cooling of the upper atmosphere.

The present study is devoted to the influence of variable temperature, density and viscosity caused by SA variations on the propagation of AGWs from the lower atmosphere to the thermosphere. However, solar activity may also change the thermospheric mean winds and circulation, ion viscosity, ion density and other parameters, which may influence the propagation of AGWs at ionospheric heights. Therefore, further numerical modeling and studies are essential for better knowledge of the SA influence on characteristics of AGWs propagating in the thermosphere. Such modeling might be helpful for advances in parameterizations of dynamical and thermal AGW impacts in the models of atmospheric general circulation (e.g., [Yigit and Medvedev, 2010](#)).

## Funding

This study was funded by the Russian Foundation for Basic Research (grant #17-05-00458), and by the Ministry of Education and Science of Russian Federation (contract 3.1127.2014/K).

## Declaration of competing interest

The authors declare that they have no known competing financial interests or personal relationships that could have appeared to influence the work reported in this paper.

## Acknowledgements

Data obtained in the SPbU resource center “Geomodel” has been used.

## References

- Akmaev, R.A., 2007. On the energetics of the mean-flow interactions with thermally dissipating gravity waves. *J. Geophys. Res.* 112, D11125 <https://doi.org/10.1029/2006jd007908>.
- Andreassen, O., Hvidsten, O., Fritts, D., Arendt, S., 1998. Vorticity dynamics in a breaking internal gravity wave. Part 1. Initial instability evolution. *J. Fluid Mech.* 367, 27–46. <https://doi.org/10.1017/S0022112098001645>.
- AtmoSym, 2016. Multi-scale Atmosphere Model from the Earth's Surface up to 500 Km. <http://atmos.kantiana.ru/>. (Accessed 25 February 2018).
- Baker, D., Schubert, G., 2000. Convectively generated internal gravity waves in the lower atmosphere of Venus. Part II: mean wind shear and wavenumber flow interaction. *J. Atmos. Sci.* 57, 200–215. [https://doi.org/10.1175/1520-0469\(2000\)057<0200:CGIGWI>2.0.CO;2](https://doi.org/10.1175/1520-0469(2000)057<0200:CGIGWI>2.0.CO;2).
- Djuth, F.T., Sulzer, M.P., Gonzales, S.A., Mathews, J.D., Elder, J.H., Walterscheid, R.L., 2004. A continuum of gravity waves in the Arcibo thermosphere. *J. Geophys. Res.* 31, L16801. <https://doi.org/10.1029/2003GL019376>.
- Francis, S.H., 1973. Acoustic-gravity modes and large-scale traveling ionospheric disturbances of a realistic, dissipative atmosphere. *J. Geophys. Res.* 78, 2278–2301. <https://doi.org/10.1029/JA078i013p02278>.
- Fritts, D.C., Alexander, M.J., 2003. Gravity wave dynamics and effects in the middle atmosphere. *Rev. Geophys.* 41 (1), 1003. <https://doi.org/10.1029/2001RG000106>.
- Fritts, D.C., Garten, J.F., Andreassen, O., 1996. Wave braking and transition to turbulence in stratified shear flows. *J. Atmos. Sci.* 53 (8), 1057–1085. [https://doi.org/10.1175/1520-0469\(1996\)053<1057:WBATT>2.0.CO;2](https://doi.org/10.1175/1520-0469(1996)053<1057:WBATT>2.0.CO;2).
- Fritts, D.C., Vadas, S.L., 2008. Gravity wave penetration into the thermosphere: sensitivity to solar variations and mean winds. *Ann. Geophys.* 26, 3841–3861. <https://doi.org/10.5194/angeo-26-3841-2008>.

- Fritts, D.C., Vadas, S.L., Wan, K., Werne, J.A., 2006. Mean and variable forcing of the middle atmosphere by gravity waves. *J. Atmos. Sol. Terr. Phys.* 68, 247–265. <https://doi.org/10.1016/j.jastp.2005.04.010>.
- Fritts, D.C., Wang, L., Werne, J., Lund, T., Wan, K., 2009. Gravity wave instability dynamics at high Reynolds numbers. Part II: turbulence evolution, structure, and anisotropy. *J. Atmos. Sci.* 66, 1149–1171. <https://doi.org/10.1175/2008JAS2727.1>.
- Fritts, D.C., Franke, P.M., Wan, K., Lund, T., Werne, J., 2011. Computation of clear-air radar backscatter from numerical simulations of turbulence: 2. Backscatter moments throughout the lifecycle of a Kelvin-Helmholtz instability. *J. Geophys. Res.* 116, D11105. <https://doi.org/10.1029/2010JD014618>.
- Gavrilov, N.M., 1990. Parameterization of accelerations and heat flux divergences produced by internal gravity waves in the middle atmosphere. *J. Atmos. Terr. Phys.* 52 (9), 707–713. [https://doi.org/10.1016/0021-9169\(90\)90003-6](https://doi.org/10.1016/0021-9169(90)90003-6).
- Gavrilov, N.M., 1995. Distributions of the intensity of ion temperature perturbations in the thermosphere. *J. Geophys. Res.* 100 (A12), 23835–23844. <https://doi.org/10.1029/95JA01927>.
- Gavrilov, N.M., 2007. Structure of the mesoscale variability of the troposphere and stratosphere found from radio refraction measurements via CHAMP satellite. *Izvestiya Atmos. Ocean. Phys.* 43 (4), 451–460. <https://doi.org/10.1134/S000143380704007X>.
- Gavrilov, N.M., Fukao, S., 1999. A comparison of seasonal variations of gravity wave intensity observed by the MU radar with a theoretical model. *J. Atmos. Sci.* 56, 3485–3494. [https://doi.org/10.1175/1520-0469\(1999\)056<3485:ACOSVO>2.0.CO;2](https://doi.org/10.1175/1520-0469(1999)056<3485:ACOSVO>2.0.CO;2).
- Gavrilov, N.M., Kshevetskii, S.P., 2013a. Numerical modeling of propagation of breaking nonlinear acoustic-gravity waves from the lower to the upper atmosphere. *Adv. Space Res.* 51 (7), 1168–1174. <https://doi.org/10.1016/j.asr.2012.10.023>.
- Gavrilov, N.M., Kshevetskii, S.P., 2013b. A study of propagation of nonlinear acoustic-gravity waves in the middle and upper atmosphere by means of numerical modeling. *Russ. J. Phys. Chem. (Engl. Transl.) B* 7 (6), 788–794. <https://doi.org/10.1134/S1990793113050163>.
- Gavrilov, N.M., Kshevetskii, S.P., 2014a. Numerical modeling of the propagation of nonlinear acoustic-gravity waves in the middle and upper atmosphere. *Izvestiya Atmos. Ocean. Phys.* 50, 66–72. <https://doi.org/10.1134/S0001433813050046>.
- Gavrilov, N.M., Kshevetskii, S.P., 2014b. Three-dimensional numerical simulation of nonlinear acoustic-gravity wave propagation from the troposphere to the thermosphere. *Earth Planets Space* 66, 88. <https://doi.org/10.1186/1880-5981-66-88>.
- Gavrilov, N.M., Kshevetskii, S.P., 2015. Dynamical and thermal effects of nonsteady nonlinear acoustic-gravity waves propagating from tropospheric sources to the upper atmosphere. *Adv. Space Res.* 55 <https://doi.org/10.1016/j.asr.2015.01.033>.
- Gavrilov, N.M., Shved, G.M., 1975. Attenuation of acoustic-gravity waves in an anisotropically turbulent, radiating atmosphere. *Izvestiya Atmos. Ocean. Phys.* 11 (7), 681–689.
- Gavrilov, N.M., Richmond, A.D., Bertin, F., Lafeuille, M., 1994. Investigation of seasonal and interannual variations of internal gravity waves in the thermosphere over Saint-Cantin. *J. Geophys. Res.* 99 (A4), 6297–6306. <https://doi.org/10.1029/93JA03164>.
- Gavrilov, N.M., Kshevetskii, S.P., Koval, A.V., 2018. Propagation of non-stationary acoustic-gravity waves at thermospheric temperatures corresponding to different solar activity. *J. Atmos. Sol. Terr. Phys.* 172, 100–106. <https://doi.org/10.1016/j.jastp.2018.03.021>.
- Gossard, E.E., Hooke, W.H., 1975. *Waves in the Atmosphere*. Elsevier Sci. Publ. Co., Amsterdam-Oxford-New York.
- Hickey, M.P., 1987. A theoretical comparison of internal gravity wave propagation and dissipation in high and low temperature thermospheres: implications for orbiting spacecraft. In: *Paper Presented at 25th Aerospace Sciences Meeting*. Am. Inst. of Aeronaut. and Astronaut., Reno, Nev.
- Hickey, M.P., Schubert, G., Walterscheid, R.L., 2001. Acoustic wave heating of the thermosphere. *J. Geophys. Res.* 106 (A10), 21543–21548. <https://doi.org/10.1029/2001JA000036>.
- Hickey, M.P., Walterscheid, R.L., Schubert, G., 2011. Gravity wave heating and cooling of the thermosphere: sensible heat flux and viscous flux of kinetic energy. *J. Geophys. Res.* 116, A12326. <https://doi.org/10.1029/2011JA016792>.
- Karpov, I.V., Kshevetskii, S.P., 2014. Formation of large-scale disturbances in the upper atmosphere caused by acoustic gravity wave sources on the Earth's surface. *Geomagn. Aeron.* 54 (4), 553–562. <https://doi.org/10.1134/S0016793214040173>.
- Kikoin, I.K., 1976. *Tables of Physical Quantities*. ed. Atomizdat Press, Moscow, pp. 272–279.
- Klausner, V., Fagundes, P.R., Sahai, Y., Wrasse, C.M., Pillat, V.G., Becker-Guedes, F., 2009. Observations of GW/TID oscillations in the F2 layer at low latitude during high and low solar activity, geomagnetic quiet and disturbed periods. *J. Geophys. Res.* 114, A02313. <https://doi.org/10.1029/2008JA013448>.
- Kshevetskii, S.P., Gavrilov, N.M., 2005. Vertical propagation, breaking and effects of nonlinear gravity waves in the atmosphere. *J. Atmos. Sol. Terr. Phys.* 67 (11), 1014–1030. <https://doi.org/10.1016/j.jastp.2005.02.013>.
- Lin, C.Y., Deng, Y., Sheng, C., Drob, D.P., 2017. A study of the nonlinear response of the upper atmosphere to episodic and stochastic acoustic-gravity wave forcing. *J. Geophys. Res. Space Physics* 122. <https://doi.org/10.1002/2016JA022930>, 1178–119.
- Liu, X., Xu, J., Liu, H.-L., Ma, R., 2008. Nonlinear interactions between gravity waves with different wavelengths and diurnal tide. *J. Geophys. Res.* 113, D08112. <https://doi.org/10.1029/2007JD009136>.
- Liu, X., Xu, J., Gao, H., Chen, G., 2009. Kelvin-Helmholtz billows and their effects on mean state during gravity wave propagation. *Ann. Geophys.* 27, 2789–2798. <https://doi.org/10.5194/angeo-27-2789-2009>.

- Medvedev, A.S., Gavrilov, N.M., 1995. The nonlinear mechanism of gravity wave generation by meteorological motions in the atmosphere. *J. Atmos. Terr. Phys.* 57, 1221–1231. [https://doi.org/10.1016/0021-9169\(95\)00008-P](https://doi.org/10.1016/0021-9169(95)00008-P).
- Medvedev, A.S., Klaassen, P., 2003. Thermal effects of saturating gravity waves in the atmosphere. *J. Geophys. Res.* 108 (D2), 4040. <https://doi.org/10.1029/2002JD002504>.
- Medvedev, A.S., Yiğit, E., Kuroda, T., Hartogh, P., 2013. General circulation modeling of the Martian upper atmosphere during global dust storms. *J. Geophys. Res. Planets* 118. <https://doi.org/10.1002/jgre.20163>.
- Park, J., Lühr, H., Lee, C., Kim, Y.H., Jee, G., Kim, J.-H., 2014. A climatology of medium-scale gravity wave activity in the midlatitude/low-latitude daytime upper thermosphere as observed by CHAMP. *J. Geophys. Res. Space Phys.* 119 <https://doi.org/10.1002/2013JA019705>.
- Picone, J.M., Hedin, A.E., Drob, D.P., Aikin, A.C., 2002. NRLMISE-00 empirical model of the atmosphere: statistical comparisons and scientific issues. *J. Geophys. Res.* 107 (A12), 1468. <https://doi.org/10.1029/2002JA009430>.
- Richmond, A.D., 1978. Gravity wave generation, propagation, and dissipation in the thermosphere. *J. Geophys. Res.* 83, 4131–4145. <https://doi.org/10.1029/JA083iA09p04131>.
- Snively, J.B., Pasko, V.P., 2008. Excitation of ducted gravity waves in the lower thermosphere by tropospheric sources. *J. Geophys. Res.* 113, A06303. <https://doi.org/10.1029/2007JA012693>.
- Townsend, A.A., 1965. Excitation of internal waves by a turbulent boundary layer. *J. Fluid Mech.* 22, 241–252. <https://doi.org/10.1017/S002211206500071X>.
- Townsend, A.A., 1966. Internal waves produced by a convective layer. *J. Fluid Mech.* 24, 307–319. <https://doi.org/10.1017/S0022112066000661>.
- Vadas, S.L., 2007. Horizontal and vertical propagation of gravity waves in the thermosphere from lower atmospheric and thermospheric sources. *J. Geophys. Res.* 112, A06305. <https://doi.org/10.1029/2006JA011845>.
- Vadas, S.L., Fritts, D.C., 2006. Influence of solar variability on gravity wave structure and dissipation in the thermosphere from tropospheric convection. *J. Geophys. Res.* 111, A10S12. <https://doi.org/10.1029/2005JA011510>.
- Walterscheid, R.L., Hickey, M.P., 2011. Group velocity and energy flux in the thermosphere: limits on the validity of group velocity in a viscous atmosphere. *J. Geophys. Res.* 116, D12101. <https://doi.org/10.1029/2010JD014987>.
- Yiğit, E., Medvedev, A.S., 2009. Heating and cooling of the thermosphere by internal gravity waves. *Geophys. Res. Lett.* 36, L14807. <https://doi.org/10.1029/2009GL038507>.
- Yiğit, E., Medvedev, A.S., 2010. Internal gravity waves in the thermosphere during low and high solar activity: simulation study. *J. Geophys. Res.* 115, A00G02. <https://doi.org/10.1029/2009JA015106>.
- Yiğit, E., Medvedev, A.S., 2012. Gravity waves in the thermosphere during a sudden stratospheric warming. *Geophys. Res. Lett.* 39, L21101. <https://doi.org/10.1029/2012GL053812>.
- Yiğit, E., Medvedev, A.S., 2015. Internal wave coupling processes in Earth's atmosphere. *Adv. Space Res.* 55 (4) <https://doi.org/10.1016/j.asr.2014.11.020>.
- Yiğit, E., Medvedev, A.S., 2016. Role of gravity waves in vertical coupling during sudden stratospheric warmings. *Geosci. Lett.* 3, 27. <https://doi.org/10.1186/s40562-016-0056-1>.
- Yiğit, E., Medvedev, A.S., 2017. Influence of parameterized small-scale gravity waves on the migrating diurnal tide in Earth's thermosphere. *J. Geophys. Res. Space Physics* 122. <https://doi.org/10.1002/2017JA024089>.
- Yiğit, E., Aylward, A.D., Medvedev, A.S., 2008. Parameterization of the effects of vertically propagating gravity waves for thermosphere general circulation models: sensitivity study. *J. Geophys. Res.* 113, D19106. <https://doi.org/10.1029/2008JD010135>.
- Yiğit, E., Medvedev, A.S., Aylward, A.D., Ridley, A.J., Harris, M.J., Moldwin, M.B., Hartogh, P., 2012a. Dynamical effects of internal gravity waves in the equinoctial thermosphere. *J. Atmos. Sol. Terr. Phys.* <https://doi.org/10.1016/j.jastp.2011.11.014>.
- Yiğit, E., Ridley, A.J., Moldwin, M.B., 2012b. Importance of capturing heliospheric variability for studies of thermospheric vertical winds. *J. Geophys. Res.* 117, A07306. <https://doi.org/10.1029/2012JA017596>.
- Yiğit, E., Medvedev, A.S., England, S.L., Immel, T.J., 2014. Simulated variability of the high-latitude thermosphere induced by small-scale gravity waves during a sudden stratospheric warming. *J. Geophys. Res.* 119 <https://doi.org/10.1002/2013JA019283>.
- Yiğit, E., Medvedev, A.S., Hartogh, P., 2015a. Gravity waves and high-altitude CO<sub>2</sub> ice cloud formation in the Martian atmosphere. *Geophys. Res. Lett.* 42 <https://doi.org/10.1002/2015GL064275>.
- Yiğit, E., England, S.L., Liu, G., Medvedev, A.S., Mahaffy, P.R., Kuroda, T., Jakosky, B.M., 2015b. High-altitude gravity waves in the Martian thermosphere observed by MAVEN/NGIMS and modeled by a gravity wave scheme. *Geophys. Res. Lett.* 42 <https://doi.org/10.1002/2015GL065307>.
- Yu, Y., Hickey, M.P., 2007. Numerical modeling of a gravity wave packet ducted by the thermal structure of the atmosphere. *J. Geophys. Res.* 112, A06308. <https://doi.org/10.1029/2006JA012092>.